GDCh Research Article Angewandte International Edition Chemie www.angewandte.org

How to cite: *Angew. Chem. Int. Ed.* **2026**, *65*, e24293
doi.org/10.1002/anie.202524293

Organic Light-Emitting Diodes Hot Paper

Spiro-fluoreno-imidazole (SFI) Emitters Efficiently Harvesting Hot Excitons for Deep-Blue Organic Light-Emitting Diodes with CIE_y Below 0.046

*Songkun Zeng, Yufeng Xie, Wenbin Huang, Chenlong Wei, Yantao Deng, Peng Zou, Chao Li, Teng-Teng Chen, Zujin Zhao, and Zikai He**

Abstract: Hot exciton emitters have emerged as promising candidates for efficient deep-blue fluorescent organic light-emitting diodes (OLEDs), by enabling triplet exciton harvesting through high-lying reverse intersystem crossing. However, limited molecular catalogues impede comprehensive mechanistic investigations and device performance elevations. Here, for the first time, we introduced a novel rigid and steric spiro-fluoreno-fused imidazole (SFI) skeleton to engineer high-performance deep-blue hot exciton emitters. Three derivatives, Cz-SFI, tCz-SFI, and 3Cz-SFI, were strategically designed to modulate donor-acceptor orbital overlap and hybridized local and charge-transfer character. Detailed theoretical calculations and transient absorption spectra clearly revealed the dominant channel of high-lying reverse intersystem crossing, with a rapid rate constant up to 3.36×10^9 s^{-1}. Remarkably, the tCz-SFI-based OLED device achieved deep-blue electroluminescence with an exciton utilization efficiency of 83.2% and an unprecedented external quantum efficiency of 12.55% by efficiently harvesting hot triplet excitons. The device exhibited stable electroluminescence peaking at 410 nm, corresponding to Commission Internationale de l'Eclairage coordinates of (0.161, 0.043), setting a new benchmark for deep-blue hot-exciton OLEDs.

Introduction

Since their first demonstration in 1987, organic light-emitting diodes (OLEDs) have achieved significant commercial success and are now widely used in full-color displays and solid-state lighting.[1] However, the performance of blue emitters in OLEDs lags far behind that of their green and red counterparts.[2,3] The situation becomes particularly acute for ultra-high definition displays requiring OLEDs to meet the BT.2020 color gamut standard defined by the International Telecommunication Union Radiocommunication Sector.[4–13] The BT.2020 standard mandates blue OLEDs with Commission Internationale de l'Éclairage (CIE) chromaticity coordinates of (0.131, 0.046), posing a significant challenge for the development of blue emitters.[14–17]

Conventional fluorescent materials are theoretically limited by quantum spin statistics, which restricts exciton utilization efficiency to a maximum of 25% due to exclusive reliance on singlet excitons.[18,19] To overcome the limitation, several innovative strategies, including thermally activated delayed fluorescence,[4,7] triplet-triplet annihilation,[20] and energy transfer (sensitizer),[5,6,8,21,22] etc., have been extensively developed. Recently, a class of "hot exciton" materials effectively harnesses triplet excitons via a high-lying reverse intersystem crossing (hRISC). The materials successfully break the traditional 25% spin-statistical limit, circumventing the quantum efficiency bottleneck.[23–32] The hybridized local and charge-transfer (HLCT) excited state characteristics have been revealed and play a vital role in molecular design. A low-lying localized excited (LE) state enhances luminescence efficiency and radiative decay rates, and a high-lying charge-transfer (CT) state facilitates triplet exciton utilization.[33–35]

Imidazole derivatives are promising hot exciton candidates due to their molecular structure, which contains both electron-rich and electron-deficient nitrogen atoms, enabling facile LE-CT modulation.[36] Consequently, modifying imidazole structures becomes a practical strategy to enhance device performance. Several representative examples have been put forth.[37–41] Notably, since Ma et al. first reported a deep-blue HLCT material based on 1-phenyl-1H-phenanthro[9,10-d]imidazole (PPI),[41] numerous blue PPI derivatives have been explored. Now, it stands out as an ideal acceptor unit for deep-blue hot exciton emitters due to its bipolar character, molecular planarity, and high thermal stability.[42–44]

[*] S. Zeng, Y. Xie, W. Huang, C. Wei, Y. Deng, Z. He
School of Science, Harbin Institute of Technology, Shenzhen, Guangdong 518055, China
E-mail: hezikai@hit.edu.cn

P. Zou, Z. Zhao
State Key Laboratory of Luminescent Materials and Devices, Guangdong Provincial Key Laboratory of Luminescence from Molecular Aggregates, South China University of Technology, Guangzhou 510640, China

C. Li, T.-T. Chen
Department of Chemistry, The Hong Kong University of Science and Technology, Clear Water Bay, Kowloon, Hong Kong 999077, China

S. Zeng, Y. Xie, W. Huang, Z. He
School of Chemical Engineering and Technology, Harbin Institute of Technology, Harbin, Heilongjiang 150001, China

Additional supporting information can be found online in the Supporting Information section

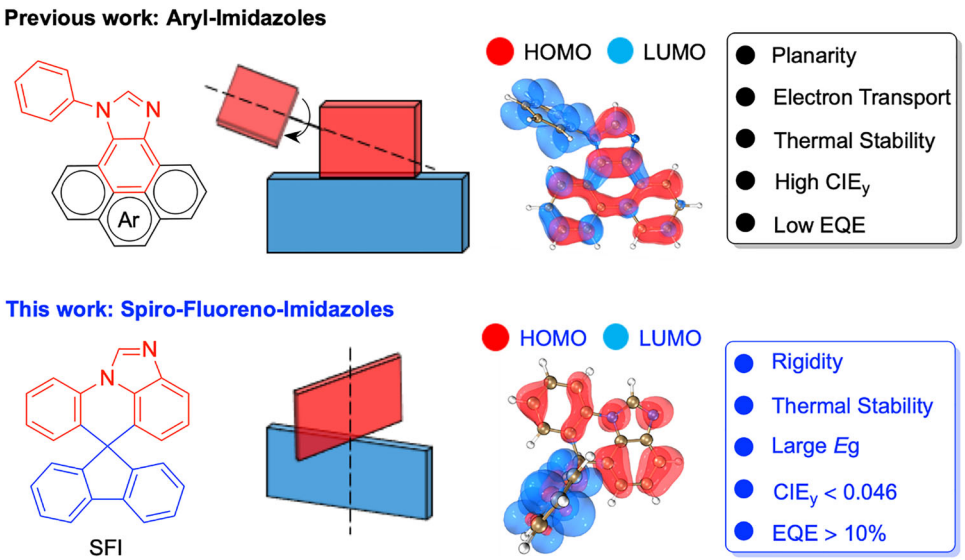

Figure 1. Previously reported aryl-imidazole emitters and the design concept for the SFI skeleton.

However, PPI-based hot exciton materials rarely achieved both the BT.2020 CIE_y coordinate requirement and an external quantum efficiency (EQE) exceeding 10% for deep-blue emitters.

In this work, a novel acceptor SFI (1′-phenylspiro[fluorene-9,6′-imidazo[4,5,1-de]acridine]) was engineered by bridging the phenyl ring and benzimidazole moiety via spirofluorene (Figure 1). SFI exhibits a larger energy gap compared to previously reported analogues, providing enhanced design flexibility for developing deep-blue emitters. Three distinct carbazole-based donors were strategically designed to modulate the CT characteristics between donor and acceptor units, thereby yielding three HLCT emitters: Cz-SFI, tCz-SFI, and 3Cz-SFI. The optimized device exhibited outstanding performance, achieving an EQE_{max} of 12.55% with CIE_y < 0.046. These results unequivocally demonstrate SFI's significant potential in developing deep-blue hot exciton fluorescent OLEDs.

Results and Discussion

Synthesis and Structural Characterization

The spiro-fluoreno-imidazole (SFI) skeletons were synthesized through an acid-catalyzed ring cyclization reaction between 2-aminodiphenylamines and fluorenone.[45] Then, a series of aryl-aldehyde donors was used to produce the target SFI derivatives through a sequential condensation reaction (Scheme 1 and Scheme S1). Detailed structural characterizations were conducted using ^1H and ^{13}C NMR spectroscopy and high-resolution MALDI-TOF mass spectrometry, as shown in Figures S1–S19. Thermal stability assessed by thermogravimetric analysis showed high decomposition temperatures (T_d, 5% weight loss) of 460 °C, 479 °C, and 525 °C for Cz-SFI, tCz-SFI, and 3Cz-SFI, respectively (Figure S20).

Single crystals of Cz-SFI suitable for X-ray diffraction analysis were obtained through slow evaporation of an ethanol solution. The crystallographic data (CCDC No.: 2486422) for Cz-SFI[46] are summarized in Table S1. A twisted molecular configuration was observed between the donor and acceptor parts, with torsional angles of 52.6° ($\theta_{A/B}$) and 53.6° ($\theta_{B/C}$), leading to a pronounced CT character. The orthogonal geometry of the spiro-skeleton was confirmed. It contributes to the high molecular rigidity, as evidenced by the calculated root-mean-square displacement (RMSD) of 0.14 Å, and effectively inhibits π-π stacking by introducing steric hindrance. The molecular configuration would suppress the exciton quenching in the aggregates.[47–49]

Theoretical Analysis of Potential hRISC

As illustrated in Figure 2a, density functional theory (DFT) calculations were first performed to determine the geometric and electronic configurations of the obtained compounds. The frontier molecular orbitals analysis revealed the distinct spatial distributions and large energy gaps of the highest occupied molecular orbitals (HOMOs) and the lowest unoccupied molecular orbitals (LUMOs). Their HOMO distribution is mainly confined to the carbazole donor framework, while LUMOs are mostly localized on the SFI acceptor moieties with partial delocalization to adjacent phenyl rings. Notably, there is significant spatial overlap between HOMO and LUMO in both Cz-SFI and tCz-SFI systems, indicating their HLCT excited states.

In contrast, 3Cz-tSFI exhibited complete spatial separation between the HOMO and LUMO orbitals, a distinctive feature of a through-space CT-type molecule. The energy gaps were found to be 3.92 eV for Cz-SFI, 3.60 eV for tCz-SFI, and 3.84 eV for 3z-SFI, respectively, indicating their potential for deep-blue emission. Furthermore, energy levels of frontier

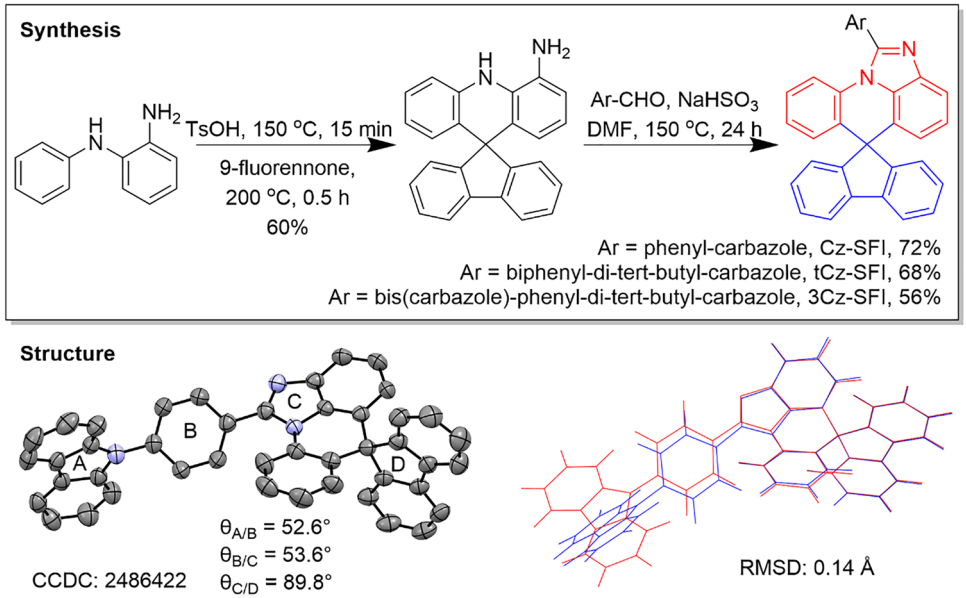

Scheme 1. A detailed synthetic route for Cz-SFI, tCz-SFI, and 3Cz-SFI, and the single crystal structure and the root mean square displacement (RMSD) for Cz-SFI.

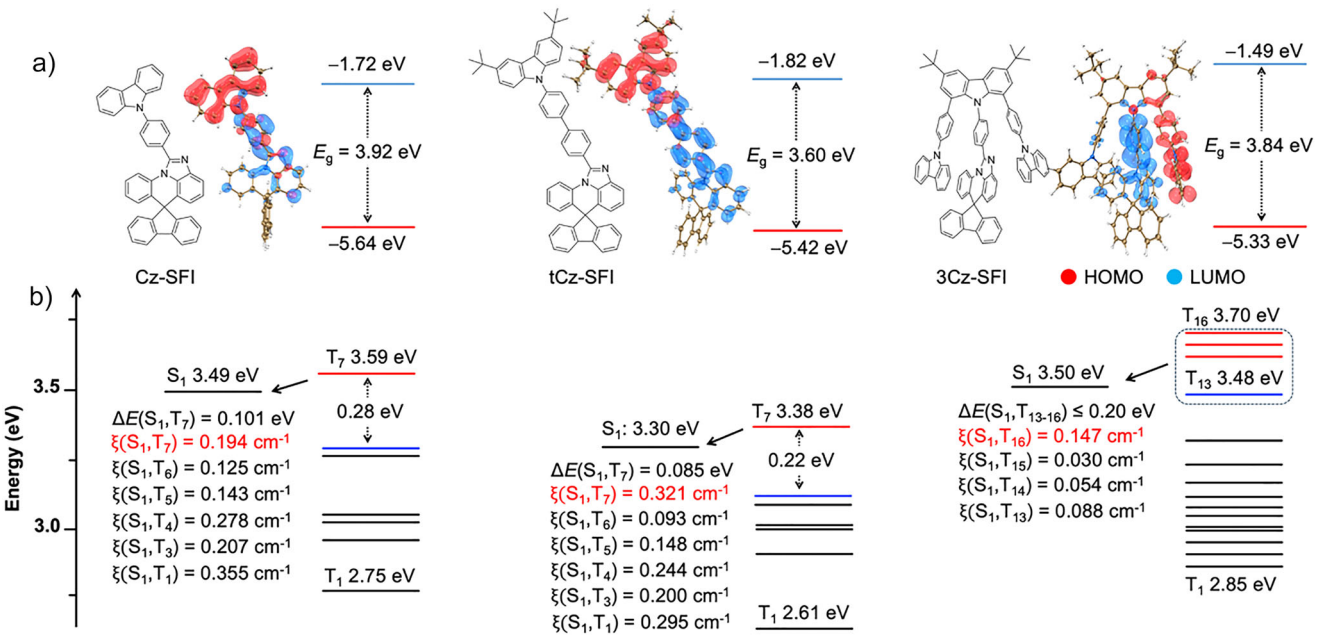

Figure 2. a) Energy levels and spatial distribution of HOMOs and LUMOs. b) Calculated energy level diagrams and spin-orbit coupling matrix elements (ξ) of excited states of Cz-SFI, tCz-SFI, and 3Cz-SFI, respectively.

molecular orbitals were determined by experimental ultraviolet photoelectron spectroscopy as −6.53/−2.87 eV for Cz-SFI, −6.32/−2.76 eV for tCz-SFI, and −6.45/−2.94 eV for 3Cz-SFI, respectively (Figure S21).

The electronic configurations of excited states of these molecules were investigated through time-dependent density functional theory (TD-DFT) calculations at the B3LYP/def2-SVP level. As shown in Figure 2b, the extended π-bridge and the enhanced electron-donating ability of the tertbutyl-carbazole unit in tCz-SFI reduce the hole-electron overlap, giving more pronounced CT character. Large singlet-triplet energy gaps (ΔE_{ST}) of 0.74, 0.69, and 0.65 eV were evaluated for Cz-SFI, tCz-SFI, and 3Cz-SFI, respectively, indicating a forbidden thermally activated RISC process from T_1 to S_1 states. Notably, for Cz-SFI and tCz-SFI, minimal energy gaps were found between the upper T_7 level and the S_1 state. 3Cz-SFI exhibited almost negligible ΔE_{ST} values between T_{13}-T_{16} and S_1 states. Besides, substantial spin-orbit coupling (SOC) matrix elements were observed in these systems, especially those high values between upper T_n states and S_1 states.

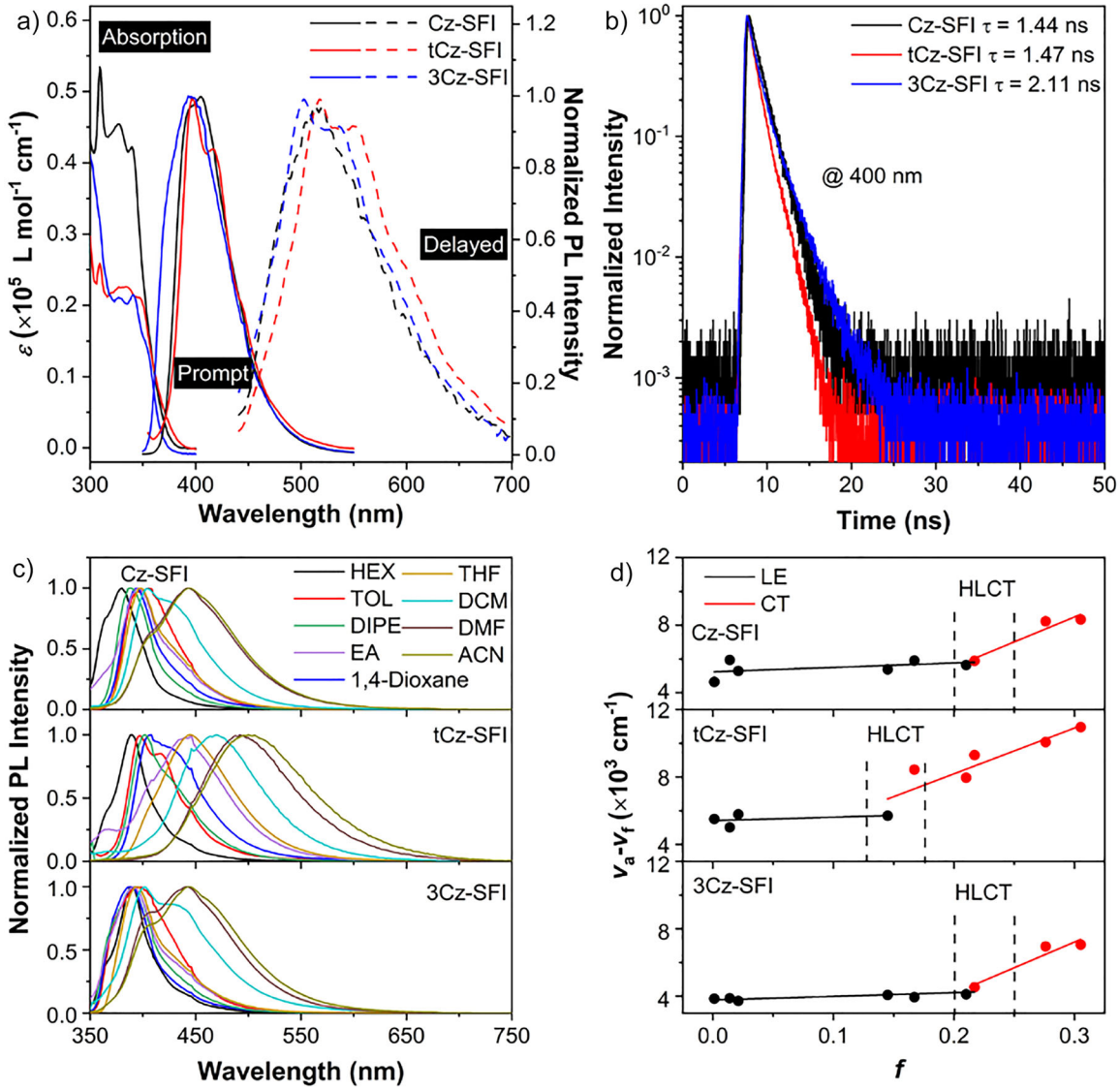

Figure 3. a) Ultraviolet-visible (UV–vis) absorption and normalized photoluminescent (PL) prompt fluorescence (solid lines) and delayed phosphorescence spectra (dashed lines, 77 K) in toluene solution (10^{-5} M). b) Time-resolved decay curves monitored at 400 nm. c) Solvatochromic PL spectra in different solvents (HEX: hexane, TOL: toluene, DIPE: diisopropyl ether, EA: ethyl acetate, THF: tetrahydrofuran, DCM: dichloromethane, DMF: *N*, *N*-dimethylformamide, ACN: acetonitrile). d) Lippert–Mataga plots of Stokes shifts against solvent polarity parameters. Excitation wavelength is 350 nm.

Subsequently, natural transition orbital (NTO) analyses of excited states were performed to clarify their transition characteristics (Figures S22–S24). In the S_1 excited states, both Cz-SFI and tCz-SFI exhibited comparable levels of hybridization, with Cz-SFI having an LE/CT ratio of about 55% LE to 45% CT, while tCz-SFI displayed increased CT characteristics with approximately 38% LE versus 62% CT. This difference stems from enhanced electron-donating ability and strategically engineered orbital overlap adjustment through the longer auxiliary diphenyl conjugated linker in tCz-SFI.[27] Relatively large SOC elements were identified in $T_7 \rightarrow S_1$ transitions. Specifically, the $T_7 \rightarrow S_1$ transitions exhibited calculated SOC values ($\langle S_1|\hat{H}_{SOC}|T_7\rangle$) of 0.194 cm^{-1} for Cz-SFI and 0.321 cm^{-1} for tCz-SFI, respectively. In contrast, 3Cz-SFI exhibited SOC elements across multiple states (S_1 and $T_{13\text{-}16}$), with values ranging from 0.088 to 0.147 cm^{-1}. These findings demonstrated the potential for facilitating the hRISC processes through $T_n \rightarrow S_1$ channels upon excitation.

Photophysical Properties and HLCT Characteristics

The UV–visible absorption and photoluminescence properties were systematically investigated in dilute toluene solutions (10^{-5} M). As depicted in Figure 3a, all compounds exhibited nearly superimposable absorption spectra in the UV range. The absorption profile is characterized by a strong $\pi \rightarrow \pi^*$ transition at 290 nm and broad $\pi \rightarrow \pi^*$ transitions from 300 to 340 nm, while the lowest-energy region

Table 1: Photophysical data of the emitters.

Emitters	λ_{abs} [a] (nm)	λ_{em} [a] (nm)	Φ_{total} [b] (%)	τ_F [a] (ns)	ΔE_{ST} [c] (eV)	E_{HOMO} [d] (eV)	E_{LUMO} [e] (eV)	E_g^{opt} [f] (eV)	$\Delta\lambda$ [g] (nm)	ΔE [g] (eV)
Cz-SFI	293, 339	406	77.4	1.44	0.88	−6.53	−2.87	3.66	64	0.47
tCz-SFI	298, 348	396	82.3	1.47	0.74	−6.32	−2.76	3.56	110	0.70
3Cz-SFI	294, 353	393	52.6	2.11	0.71	−6.45	−2.94	3.51	54	0.39

[a] Measured in 10^{-5} M toluene solution. [b] Measured in 5 wt% *m*-CPCN film. [c] Calculated from onsets of fluorescence and phosphorescence spectra. [d] Collected from UPS results. [e] Calculated from HOMO and E_g^{opt}. [f] E_g^{opt} by $E_g = E_{HOMO} - E_{LUMO}$ obtained from the onset of the UV–vis absorption spectra. [g] Calculated from different solvents.

exhibits a negligible bathochromic shift corresponding to an intramolecular charge-transfer band.[50,51] Notably, solvent-polarity-dependent absorption spectra showed a slightly bathochromic shift (Figure S25), indicating a small dipole moment in the ground states.

All emitters showed intense ultraviolet to deep-blue photoluminescence with emission peaks at 406 nm for Cz-SFI, 396 nm for tCz-SFI, and 393 nm for 3Cz-SFI in solution (Figure 3a and Table 1). In doped films, Cz-SFI and 3Cz-SFI showed emission peaks at 396 and 400 nm, respectively, similar to those in solution, while tCz-SFI exhibited a red-shifted emission peak at 426 nm. As shown in Figure 3c,d, tCz-SFI exhibits enhanced CT character than the other two compounds, which accounts for the observed redshift in the highly polar host matrix of mCPCN (Figure S26). The corresponding fluorescence lifetimes of the doped films are presented in Figure S27. These compounds achieved high photoluminescence quantum yields of 77.4%, 82.3%, and 52.6% in their doped films (Figures S28–S30). Based on the fluorescence and low-temperature (77 K) phosphorescence spectra (Figure 3a), the energy levels of S_1 and T_1 were estimated to be 3.30 eV / 2.42 eV for Cz-SFI, 3.13 eV / 2.39 eV for tCz-SFI, and 3.18 eV / 2.47 eV for 3Cz-SFI (Table 1). Therefore, the corresponding ΔE_{ST} between S_1 and T_1 was calculated as 0.88 eV for Cz-SFI, 0.74 eV for tCz-SFI, and 0.71 eV for 3Cz-SFI. The experimental values showed excellent agreement with the theoretical results. Additionally, the time-resolved PL decay curves revealed that only short single-exponential fluorescence lifetimes were observed, with values of 1.44, 1.47, and 2.11 ns for Cz-SFI, tCz-SFI, and 3Cz-SFI, respectively (Figure 3b and Table 1). Given the large ΔE_{ST} values and nanosecond-scale emission lifetimes, the RISC process from T_1 to S_1, as well as thermally activated delayed fluorescence, was blocked.

To elucidate the fundamental mechanisms, solvent-dependent PL spectra were investigated. As shown in Figure 3c, the pronounced solvatochromic effect was observed. The emission maxima displayed redshift peaks of 64 nm for Cz-SFI, 110 nm for tCz-SFI, and 54 nm for 3Cz-SFI when the solvent was changed from nonpolar hexane to polar acetonitrile. The significant solvent-dependent bathochromic shift clearly indicated the intramolecular CT characteristics of S_1 states. Among these emitters, tCz-SFI exhibited the notable CT feature, while Cz-SFI and 3Cz-SFI demonstrated similar CT behaviors. Intriguingly, all emitters showed well-defined vibronic structures in nonpolar media, in contrast to the broad and featureless emission profiles observed in high-polarity solvents. Quantitative analysis using the Lippert-Mataga model allowed the estimation of the excited-state dipole moments (μ_e) by correlating Stokes shifts (ν_a–ν_f) with solvent polarity parameters (f) (Equations S1–S4 and Tables S2–S4).[25–28] A clear biphasic linear relationship appeared (Figure 3d), indicating polarity-dependent excited-state evolution. In low-polarity solvents, the calculated μ_e values of 6.00 Debye for Cz-SFI, 5.79 Debye for tCz-SFI, and 6.84 Debye for 3Cz-SFI indicated predominant LE states. In high-polarity environments, the μ_e values increased to 13.37 Debye for Cz-SFI, 14.20 Debye for tCz-SFI, and 15.38 Debye for 3Cz-SFI, respectively, indicating CT-dominated states. The nonlinear solvatochromic effect provided compelling evidence for the existence of the hybridized local and charge transfer (HLCT) excited state in medium-polarity environments.

Transient Absorption Proofs of hRISC

The ultrafast photophysical dynamics of tCz-SFI in solution were monitored using femtosecond and nanosecond transient absorption (fs/ns-TA) spectroscopy with 340 nm excitation (pulse energy: 5.5 mW) (Figure 4 and Figures S31–S36). Within the initial 0.3–92.3 ps (Figure 4a top), the TA spectra exhibited two distinct negative signals in the 350–360 nm and 400–450 nm regions, attributed to ground-state bleaching and stimulated emission (SE, $S_1 \rightarrow S_0$ emission), respectively. Broad, positive signals observed between 360–400 nm and above 450 nm were assigned to excited-state absorption (ESA, $S_1 \rightarrow S_n$). Notably, the SE band around 400–450 nm exhibited a pronounced bathochromic shift. In comparison, the ESA signal spanning 450–700 nm exhibited an obvious hypsochromic shift. Both signal evolutions could be attributed to the conformational relaxation (**1**) of the S_1 state, which involves vibrationally relaxing from higher to lower vibrational modes. For clarity, the time-dependent SE peak maximum was plotted and fitted (Figure 4b), revealing that the SE peak shifted from 418 nm to 441 nm, accompanied by a relaxation lifetime of 3.54 ps, indicating an ultrafast solvent-stabilization process.[52] The stationary SE band was consistent with the steady-state PL spectrum of tCz-SFI in THF solution (Figure 2c). In comparison, Cz-SFI showed a similar but minor red shift (Figure S31) and a longer solvent relaxation time compared to tCz-SFI, indicating a weaker CT character of the S_1 state, which aligned with the results in Figure 2d.

Between 92.3 ps and 7.4 ns, the decay of SE signals fully coincided with the decay of ESA signals ranging from 350

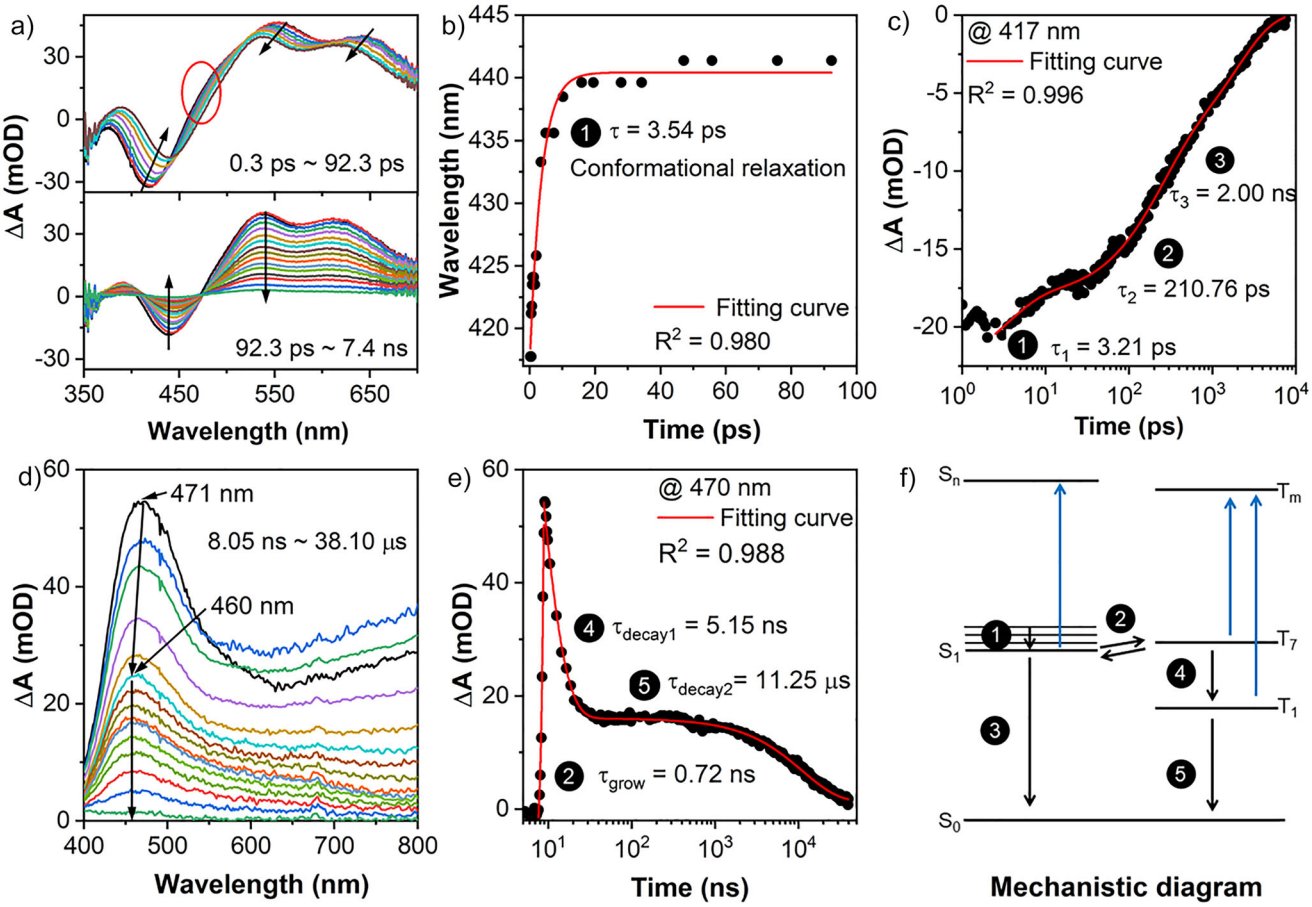

Figure 4. Transient absorption of tCz-SFI THF solution (10^{-4} M) measured at room temperature. a) Femtosecond transient absorption spectra ranging from 0.3 ps to 92.3 ps (top) and from 92.3 ps to 7400 ps (bottom). Time-dependent diagram of b) SE peaks (wavelength) from 0.3 ps to 92.3 ps and c) difference absorption signals (ΔA) monitoring at 417 nm from 92.3 ps to 7400 ps. d) Nanosecond transient absorption spectra ranging from 8.05 ns to 38.10 μs. e) Time-dependent diagram of difference absorption signals (ΔA) monitoring at 470 nm from 8.05 ns to 38.10 μs. f) Mechanistic diagram of tCz-SFI (**1**: conformational relaxation; **2**: high-lying intersystem crossing (hISC) and hRISC; **3**: fluorescence; **4**: internal conversion; **5**: phosphorescence).

to 700 nm, further indicating that these TA signals originated from the S_1 state. To investigate spectral evolution in detail, a global kinetic-fitting analysis was performed. The fs-TA kinetics of tCz-SFI at 417 nm were monitored (Figure 4c), yielding three decay lifetimes of $\tau_1 = 3.21$ ps, $\tau_2 = 210.76$ ps, and $\tau_3 = 2.00$ ns. The τ_1 lifetime corresponded to conformational relaxation and agreed with the peak wavelength simulation results in Figure 4b. The τ_3 was assigned to the fluorescence lifetime, which closely aligned with the time-resolved decay results in Figure 3b. To investigate the nature of τ_2, population changes were extracted by integrating the SE band of the differential absorption as a function of wavenumber and delay time, $\Delta A(\nu, t)$ (Equation S5 and Figures S34 and S35), yielding $\tau_1 = 2.62$ ps, $\tau_2 = 194.59$ ps, and $\tau_3 = 1.93$ ns. These values were consistent with those obtained from the kinetics fitting results at 417 nm. Based on the reported model,[53] τ_2 could be attributed to the lifetime of the dynamic equilibrium on the interconversion process of ISC and RISC.

As triplet state evolution is not fully captured in fs-TA spectroscopy, nanosecond transient absorption (ns-TA) spectroscopy was performed (Figure 4d). Initially (8.05 ns), a broad ESA band spanning 400–800 nm with a maximum at 471 nm emerged. From 8.05 ns to 16.5 ns, this peak hypsochromically shifted to 460 nm. Then, the ESA signal decayed and was completely weakened from 16.5 ns to 38.10 μs. The ns-TA decay kinetics at 470 nm were fitted with a multi-exponential function (Figure 4e), revealing three lifetimes of $\tau_{grow} = 0.72$ ns, $\tau_{decay1} = 5.15$ ns, and $\tau_{decay2} = 11.25$ μs. These lifetimes were assigned to intersystem crossing ($S_1 \rightarrow T_n$ transition), internal conversion ($T_n \rightarrow T_1$ transition), and phosphorescence decay ($T_1 \rightarrow S_0$ transition), respectively. Interestingly, a transient absorption signal around 470 nm was detected even at the early stage of the fs-TA spectra, from 0.3 ps to 92.3 ps (red cycle in Figure 4a), suggesting a possible ultrafast rate constant for the ISC process.

Based on fs/ns-TA spectra, the mechanistic diagram of tCz-SFI exciton was depicted in Figure 4f. Five distinct processes were revealed as **1** for conformational relaxation, **2** for high-lying intersystem crossing (hISC) and hRISC, **3** for fluorescence, **4** for internal conversion, and **5** for phosphorescence. According to the TA fitting lifetimes and supporting equations, the rate constants were successfully extracted and

Table 2: EL performances of devices.

Emitters	V_{on}[a)] (V)	L_{max} (cd m^{-2})	CE_{max} (cd A^{-1})	PE_{max} (lm W^{-1})	EQE_{max} (%)	Peak[b)] (nm)	CIE[b)] (x, y)	FWMH[b)] (nm)
Cz-SFI	3.4	2323.78	0.86	0.84	6.69	388	0.161, 0.035	43
tCz-SFI	3.3	838.01	3.67	3.49	12.55	410	0.161, 0.043	52
3Cz-SFI	4.0	1592.40	0.45	0.23	3.42	396	0.162, 0.038	48

[a)] Turn-on voltage at 1 cd m^{-2}. [b)] Measured at 6.0 V.

summarized in Table S5. Notably, the rate constant of reverse intersystem crossing (k_{hRISC}) was 3.36×10^9 s^{-1}, significantly higher than those of intersystem crossing $k_{hISC} = 1.39 \times 10^9$ s^{-1} and internal conversion $k_{IC} = 1.94 \times 10^8$ s^{-1} for high-lying triplet excitons. These results provided direct mechanistic evidence of the involvement of high-lying T_n states in the intersystem crossing. It also experimentally demonstrated the theoretical potential of harnessing triplet hot excitons in OLED devices by effectively competing with internal conversion.

Efficient Hot Exciton OLEDs

To evaluate the electroluminescence (EL) properties, we fabricated OLED devices with the following architecture: indium tin oxide (ITO)/MoO_3 (6 nm)/1,3-Bis(N-carbazolyl)benzene (mCP) (45 nm)/emitting layer (EML) (25 nm)/1,3,5-tris(3-pyridyl-3-phenyl)benzene (TmPyPB) (45 nm)/LiF (1 nm)/Al (100 nm), where MoO_3 and LiF served as hole and electron injection layers, respectively. mCP was used as the hole-transport layer, and TmPyPB functioned as the electron-transport layer. The EML consisted of three distinct configurations: 5 wt% Cz-SFI, tCz-SFI, or 3Cz-SFI doped in the bipolar host *m*CPCN [9-(3-(9H-carbazol-9-yl)phenyl)-9H-carbazole-3-carbonitrile]. *m*CPCN was strategically selected for its balanced hole and electron transport capabilities to maximize carrier recombination efficiency and for its ultrahigh triplet exciton energy level (>3.0 eV) to block energy transfer.[54] The detailed device architectures and molecular structures were provided in Figure S37.

All devices exhibited a low turn-on voltage of 3.3–4.0 V, illustrating the alignment between the emitters' energy levels as detected by experimental ultraviolet photoelectron spectroscopy. The maximum current efficiency (CE_{max}) of Cz-SFI, tCz-SFI, and 3Cz-SFI was 0.86, 3.67, and 0.45 cd A^{-1}, respectively, and the maximum power efficiency (PE_{max}) was 0.84, 3.49, and 0.23 lm W^{-1}. The devices present excellent performance with EQE_{max} values of 6.69%, 12.55%, and 3.42% for Cz-SFI, tCz-SFI, and 3Cz-SFI, respectively. The efficiency roll-off and low brightness observed in tCz-SFI-based devices could be attributed to an imbalance in carrier transport (Figure S38). Impressively, the doped devices exhibited deep-blue EL emission peaks at 388 nm for Cz-SFI, 410 nm for tCz-SFI, and 396 nm for 3Cz-SFI, corresponding to CIE coordinates of (0.161, 0.035), (0.161, 0.043), and (0.162, 0.038), respectively (Figure 5d,e). Notably, the tCz-SFI-based device achieved record-breaking deep-blue emission in line with the BT.2020 ultra-high-definition standard ($CIE_y \leq 0.046$), while reaching an impressive maximum EQE of 12.55%, a benchmark for deep-blue HLCT-OLEDs. These devices also exhibited good color purity, with full-width half-maximum (FWHM) values ranging from 43 to 52 nm, as summarized in Table 2. A summary of representative deep-blue OLEDs ($\lambda_{EL} \leq 430$ nm) based on hot-exciton materials is presented in Figure S39, with the corresponding device details provided in Table S6.

The TADF was first excluded based on the large singlet-triplet energy gaps (ΔE_{ST}>0.3 eV) and single-component fluorescence lifetimes in the nanosecond range. Additionally, the linear dependence of luminance on current density (Figure S40) ruled out the possibility of efficiency enhancement through triplet-triplet annihilation upconversion.[55] The exciton utilization efficiency of these emitters in the device was then calculated. The EQE of the device can be expressed by the following equation:

$$\eta_{EQE} = \gamma \times \eta_{PL} \times \eta_r \times \eta_{out} \quad (1)$$

where γ is the factor of the charge recombination efficiency (ideally assigned as 100%), η_{PL} is the PL quantum yield, η_{out} is the light out coupling efficiency, and η_r is the exciton utilization efficiency. Experimental PL quantum yields were 77.4% for 5 wt% Cz-SFI:*m*CPCN, 82.3% for 5 wt% tCz-SFI:*m*CPCN, and 52.6% for 5 wt% 3Cz-SFI:*m*CPCN. Based on the observed low horizontal dipole orientation ratio (Θ) in Figure 5f, η_{out} is should be higher than 20%. As the accurate values were difficult to calculate, we assumed a range of 20% to 30%.[21] Then, according to the previously measured PLQYs, the exciton utilization efficiency η_r values were calculated to be 29%–43% for Cz-SFI, 51%–76% for tCz-SFI, and 22%–33% for 3Cz-SFI, respectively. Additionally, based on rate constants from TA spectra fitting, the exciton utilization efficiency under electroluminescence conditions was calculated for Cz-SFI and tCz-SFI.

For S_1: the rate of formation = the rate of deactivation.

$$G_S + k_{RISC}[T] = (k_F + k_{ISC})[S] \quad (2)$$

For T_1: the rate of formation = the rate of deactivation.

$$G_T + k_{ISC}[S] = (k_{RISC} + k_{IC})[T] \quad (3)$$

For simplicity, the singlet non-radiative decay rate constant is neglected ($k_{S,nr} = 0$ s^{-1}). Based on the steady-state approximation assumption, where G_S and G_T are the singlet and triplet exciton generation fractions in electroluminescence ($G_S = 0.25$, $G_T = 0.75$), [S] and [T] can be extracted from Equations (2) and (3) as the equilibrated singlet and triplet exciton distribution. There, [S] is assigned as the

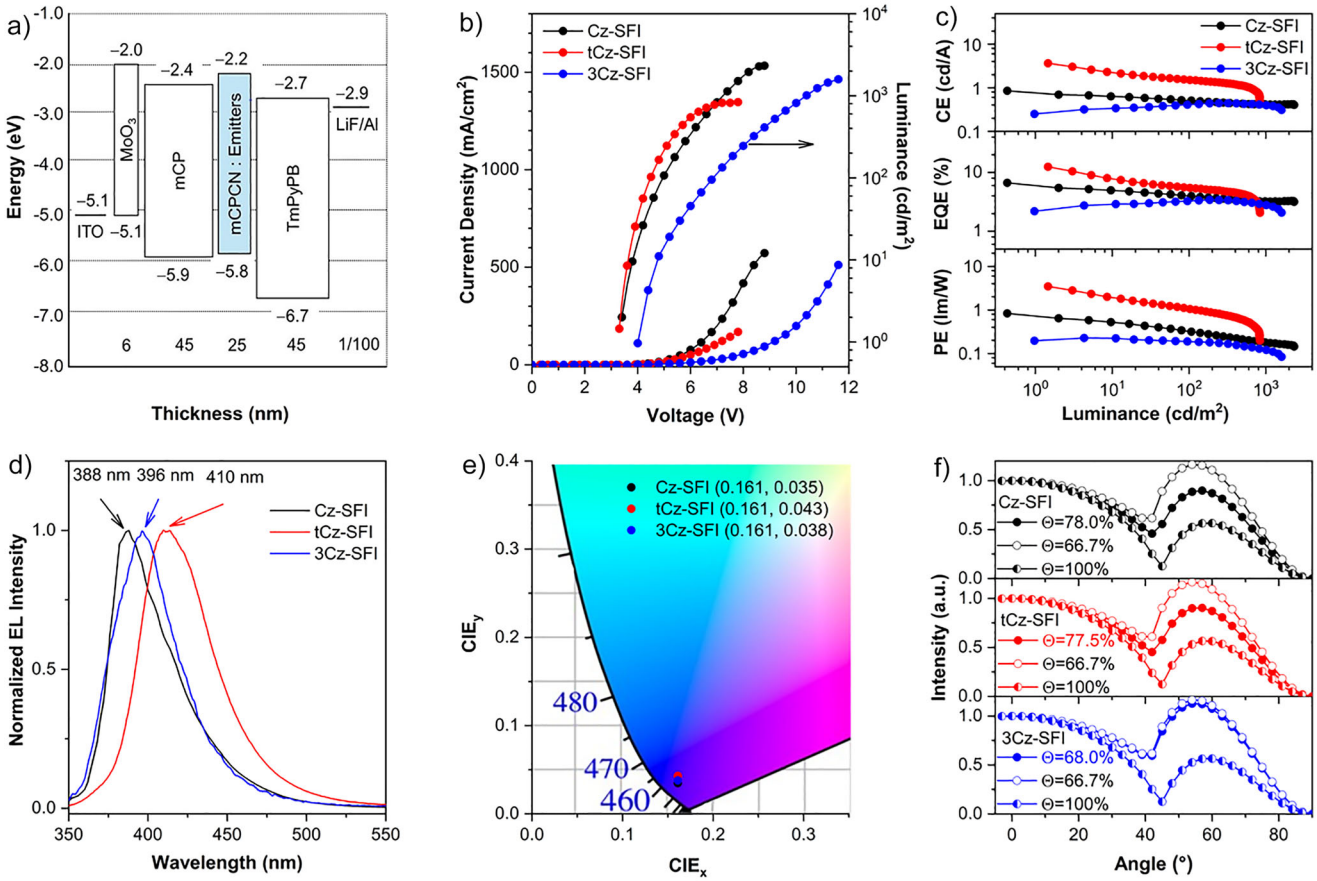

Figure 5. a) Device structure and energy level diagrams of functional layers. b) Current Density-Voltage-Luminance curves. c) CE (current efficiency)/EQE/PE (power efficiency)-Luminance curves. d) Electroluminescence spectra of devices at 6.0 V. e) CIE coordinates of the OLEDs. f) Angular-dependent PL intensity of emitters in the doped films.

exciton utilization efficiency (η_r) in an electroluminescence device, with tCz-SFI achieving a high value of 83.2% and approaching that of the OLED device (Table S5). The high η_r (> 25%) should be attributed to the conversion of high-lying triplet excitons into singlet excitons through the hRISC process. As a result, tCz-SFI surpasses the 25% spin-statistical limit for conventional fluorescent systems, unambiguously confirming hot triplet exciton harvesting capability.

Conclusion

In summary, three deep-blue emitters based on the novel spiro-fluoreno-imidazole (SFI) skeletons and carbazole-derived donors have been successfully developed and thoroughly characterized. These emitters exhibited outstanding deep-blue emission in toluene solutions. Remarkably, the dual harvesting of both singlet and triplet excitons via hRISC pathways has been unambiguously confirmed through theoretical calculations and transient absorption experiments. Femtosecond and nanosecond transient absorption spectra further revealed that tCz-SFI exhibits optimal hRISC kinetics, with rapid k_{hRISC} of 3.36×10^9 s^{-1} and slow k_{IC} of 1.94×10^8 s^{-1}. As a result, the corresponding deep-blue OLED device based on tCz-SFI achieved exceptional performance, with an EQE_{max} of 12.55% and CIE coordinates of (0.161, 0.043). This work introduces a novel SFI skeleton for efficient hot exciton harvesting, supported by detailed structure-property studies and offering a candidate for next-generation deep-blue electroluminescent materials.

Acknowledgements

This work was supported by the National Natural Science Foundation of China (22375054, 21975061), the Natural Science Foundation of Guangdong Province (2024B1515020096), and the Shenzhen Fundamental Research Program (JCYJ20241202152659001, GXWD20231130104319001).

Conflict of Interests

The authors declare no conflict of interest.

Data Availability Statement

The data that support the findings of this study are available in the Supporting Information of this article.

Keywords: Deep-blue emitter • Hot exciton • Organic light-emitting diodes • Spiro-fluoreno-imidazole • Transient absorption

[1] C. W. Tang, S. A. VanSlyke, *Appl. Phys. Lett.* **1987**, *51*, 913–915, https://doi.org/10.1063/1.98799.

[2] S. K. Jeon, H. L. Lee, K. S. Yook, J. Y. Lee, *Adv. Mater.* **2019**, *31*, e1803524, https://doi.org/10.1002/adma.201803524.

[3] Q. Y. Meng, R. Wang, Y. L. Wang, X. W. Guo, Y. Q. Liu, X. L. Wen, C. Y. Yao, J. Qiao, *Nat. Commun.* **2023**, *14*, 3927, https://doi.org/10.1038/s41467-023-39697-7.

[4] D. H. Ahn, S. W. Kim, H. Lee, I. J. Ko, D. Karthik, J. Y. Lee, J. H. Kwon, *Nat. Photonics* **2019**, *13*, 540–546, https://doi.org/10.1038/s41566-019-0415-5.

[5] L. Ge, W. Zhang, Y. H. Hao, M. Li, Y. Liu, M. Zhou, L. S. Cui, *J. Am. Chem. Soc.* **2024**, *146*, 32826–32836, https://doi.org/10.1021/jacs.4c13375.

[6] T. Hua, X. Cao, J. Miao, X. Yin, Z. Chen, Z. Huang, C. Yang, *Nat. Photonics* **2024**, *18*, 1161–1169, https://doi.org/10.1038/s41566-024-01508-w.

[7] Y. Kondo, K. Yoshiura, S. Kitera, H. Nishi, S. Oda, H. Gotoh, Y. Sasada, M. Yanai, T. Hatakeyama, *Nat. Photonics* **2019**, *13*, 678–682, https://doi.org/10.1038/s41566-019-0476-5.

[8] H. L. Lee, J. Kang, J. Lim, S. C. Kim, S. O. Jeon, J. Y. Lee, *Nat. Commun.* **2023**, *14*, 4818, https://doi.org/10.1038/s41467-023-40481-w.

[9] D. Liu, J. De, H. Gao, S. Ma, Q. Ou, S. Li, Z. Qin, H. Dong, Q. Liao, B. Xu, Q. Peng, Z. Shuai, W. Tian, H. Fu, X. Zhang, Y. Zhen, W. Hu, *J. Am. Chem. Soc.* **2020**, *142*, 6332–6339, https://doi.org/10.1021/jacs.0c00871.

[10] S. M. Suresh, L. Zhang, T. Matulaitis, D. Hall, C. Si, G. Ricci, A. M. Z. Slawin, S. Warriner, D. Beljonne, Y. Olivier, I. D. W. Samuel, E. Zysman-Colman, *Adv. Mater.* **2023**, *35*, e2300997, https://doi.org/10.1002/adma.202300997.

[11] R. W. Weerasinghe, S. Madayanad Suresh, D. Hall, T. Matulaitis, A. M. Z. Slawin, S. Warriner, Y. T. Lee, C. Y. Chan, Y. Tsuchiya, E. Zysman-Colman, C. Adachi, *Adv. Mater.* **2024**, *36*, e2402289, https://doi.org/10.1002/adma.202402289.

[12] Z. G. Wu, Y. Xin, C. Lu, W. Huang, H. Xu, X. Liang, X. Cao, C. Li, D. Zhang, Y. Zhang, L. Duan, *Angew. Chem. Int. Ed.* **2024**, *63*, e202318742, https://doi.org/10.1002/anie.202318742.

[13] Y. C. Cheng, X. Tang, R. Walia, T. Y. Zhang, X. C. Fan, J. Yu, K. Wang, C. Adachi, X. K. Chen, X. H. Zhang, *Adv. Mater.* **2025**, *37*, e2500010.

[14] P. Ma, Y. Chen, Y. Man, Q. Qi, Y. Guo, H. Wang, Z. Li, P. Chang, C. Qu, C. Han, H. Xu, *Angew. Chem. Int. Ed.* **2024**, *63*, e202316479, https://doi.org/10.1002/anie.202316479.

[15] X. F. Song, S. Luo, N. Li, X. Wan, J. Miao, Y. Zou, K. Li, C. Yang, *Angew. Chem. Int. Ed.* **2025**, *64*, e202413536, https://doi.org/10.1002/anie.202413536.

[16] C. Cao, Z.-L. Zhu, S.-J. Xian, J. Miao, S.-Y. He, H.-J. Tan, M. Xing, H. Liu, M. Yang, T. Hua, W. Xie, C. Yang, *Angew. Chem. Int. Ed.* **2025**, *64*, e202518651, https://onlinelibrary.wiley.com/doi/abs/10.1002/anie.202518651.

[17] H. Zhang, G. Li, X. Guo, K. Zhang, B. Zhang, X. Guo, Y. Li, J. Fan, Z. Wang, D. Ma, B. Z. Tang, *Angew. Chem. Int. Ed.* **2021**, *60*, 22241–22247, https://doi.org/10.1002/anie.202108540.

[18] A. C. Tadle, K. A. El Roz, C. H. Soh, D. Sylvinson Muthiah Ravinson, P. I. Djurovich, S. R. Forrest, M. E. Thompson, *Adv. Funct. Mater.* **2021**, *31*, 2101175, https://doi.org/10.1002/adfm.202101175.

[19] H. Zhang, S. Zeng, Q. Zhong, J. Huang, X. Gan, W. Zheng, Y. Wang, X. Wu, W. Zhu, *Org. Electron.* **2023**, *122*, 106903, https://doi.org/10.1016/j.orgel.2023.106903.

[20] H. Lim, S. J. Woo, Y. H. Ha, Y. H. Kim, J. J. Kim, *Adv. Mater.* **2022**, *34*, e2100161, https://doi.org/10.1002/adma.202100161.

[21] G. Pan, Z. Wu, Z. Liu, B. Xu, W. Tian, *Angew. Chem. Int. Ed.* **2023**, *62*, e202303152.

[22] R. Du, P. Ma, Y. Man, Y. Pang, C. Duan, C. Han, J. Zhang, C. Cao, Y. Wei, X. Shui, H. Xu, *Aggregate* **2023**, *4*, e390.

[23] J. Chen, H. Liu, J. Guo, J. Wang, N. Qiu, S. Xiao, J. Chi, D. Yang, D. Ma, Z. Zhao, B. Z. Tang, *Angew. Chem. Int. Ed.* **2022**, *61*, e202116810, https://doi.org/10.1002/anie.202116810.

[24] C. Du, H. Liu, Z. Cheng, S. Zhang, Z. Qu, D. Yang, X. Qiao, Z. Zhao, P. Lu, *Adv. Funct. Mater.* **2023**, *33*, 2304854.

[25] G. Li, K. Xu, J. Zheng, X. Fang, W. Lou, F. Zhan, C. Deng, Y. F. Yang, Q. Zhang, Y. She, *J. Am. Chem. Soc.* **2024**, *146*, 1667–1680, https://doi.org/10.1021/jacs.3c12517.

[26] X. Guo, P. Yuan, J. Fan, X. Qiao, D. Yang, Y. Dai, Q. Sun, A. Qin, B. Z. Tang, D. Ma, *Adv. Mater.* **2021**, *33*, e2006953, https://doi.org/10.1002/adma.202006953.

[27] C. Liao, B. Chen, Q. Xie, X. Li, H. Liu, S. Wang, *Adv. Mater.* **2023**, *35*, e2305310, https://doi.org/10.1002/adma.202305310.

[28] B. Ma, B. Zhang, H. Zhang, Y. Huang, L. Liu, B. Wang, D. Yang, D. Ma, B. Z. Tang, Z. Wang, *Adv. Sci.* **2024**, *11*, e2407254.

[29] R. Wang, T. Li, C. Liu, M. Xie, H. Zhou, Q. Sun, B. Yang, S. T. Zhang, S. Xue, W. Yang, *Adv. Funct. Mater.* **2022**, *32*, 2201143, https://doi.org/10.1002/adfm.202201143.

[30] Y. Xu, X. Liang, X. Zhou, P. Yuan, J. Zhou, C. Wang, B. Li, D. Hu, X. Qiao, X. Jiang, L. Liu, S. J. Su, D. Ma, Y. Ma, *Adv. Mater.* **2019**, *31*, e1807388.

[31] Y. Xu, P. Xu, D. Hu, Y. Ma, *Chem. Soc. Rev.* **2021**, *50*, 1030–1069, https://doi.org/10.1039/D0CS00391C.

[32] S. Zeng, C. Xiao, J. Zhou, Q. Dong, Q. Li, J. Lim, H. Ma, J. Y. Lee, W. Zhu, Y. Wang, *Adv. Funct. Mater.* **2022**, *32*, 2113183.

[33] Y. Gao, S. Zhang, Y. Pan, L. Yao, H. Liu, Y. Guo, Q. Gu, B. Yang, Y. Ma, *Phys. Chem. Chem. Phys.* **2016**, *18*, 24176–24184, https://doi.org/10.1039/C6CP02778D.

[34] L. Jiang, B. Wang, L. Zhu, W. Tan, H. Gan, Y. Yu, Y. Ma, *J. Phys. Chem. Lett.* **2025**, *16*, 6914–6918, https://doi.org/10.1021/acs.jpclett.5c01184.

[35] H. Zhang, B. Zhang, Y. Zhang, Z. Xu, H. Wu, P. A. Yin, Z. Wang, Z. Zhao, D. Ma, B. Z. Tang, *Adv. Funct. Mater.* **2020**, *30*, 2002323, https://doi.org/10.1002/adfm.202002323.

[36] W. C. Chen, Z. L. Zhu, C. S. Lee, *Adv. Opt. Mater.* **2018**, *6*, 1800258, https://doi.org/10.1002/adom.201800258.

[37] M. Liu, X. L. Li, D. C. Chen, Z. Xie, X. Cai, G. Xie, K. Liu, J. Tang, S. J. Su, Y. Cao, *Adv. Funct. Mater.* **2015**, *25*, 5190–5198, https://doi.org/10.1002/adfm.201502163.

[38] G. X. Yang, D. H. Liu, Q. Gu, X. Peng, D. L. Li, M. Li, M. Liu, J. Chen, K. Liu, S. J. Su, *Adv. Opt. Mater.* **2023**, *11*, 2300455, https://doi.org/10.1002/adom.202300455.

[39] H. Liu, L. Kang, J. Li, F. Liu, X. He, S. Ren, X. Tang, C. Lv, P. Lu, *J. Mater. Chem. C* **2019**, *7*, 10273–10280, https://doi.org/10.1039/C9TC02990G.

[40] T. Jiang, J. Qin, J. Lin, X. Lin, W. Liu, Z. Xie, C. Redshaw, Z. Zhao, X. Feng, *ACS Appl. Mater. Interfaces* **2025**, *17*, 43339–43351, https://doi.org/10.1021/acsami.5c08493.

[41] W. Li, Y. Pan, R. Xiao, Q. Peng, S. Zhang, D. Ma, F. Li, F. Shen, Y. Wang, B. Yang, Y. Ma, *Adv. Funct. Mater.* **2014**, *24*, 1609–1614, https://doi.org/10.1002/adfm.201301750.

[42] C. Cao, G. X. Yang, J. H. Tan, D. Shen, W. C. Chen, J. X. Chen, J. L. Liang, Z. L. Zhu, S. H. Liu, Q. X. Tong, C. S. Lee, *Mater. Today Energy* **2021**, *21*, 100727, https://doi.org/10.1016/j.mtener.2021.100727.

[43] H. Liu, X. Tang, Z. Cheng, Y. Hu, Y. Yan, Y. Xu, Z. Su, F. Liu, P. Lu, *Chin. Chem. Lett.* **2024**, *35*, 109809, https://doi.org/10.1016/j.cclet.2024.109809.

[44] H. Zhang, J. Xue, C. Li, S. Zhang, B. Yang, Y. Liu, Y. Wang, *Adv. Funct. Mater.* **2021**, *31*, 2100704, https://doi.org/10.1002/adfm.202100704.
[45] H. Liu, Z. Liu, G. Li, H. Huang, C. Zhou, Z. Wang, C. Yang, *Angew. Chem. Int. Ed.* **2021**, *60*, 12376–12380, https://doi.org/10.1002/anie.202103187.
[46] Deposition number 2486422 contains the supplementary crystallographic data for CZ-SFI. These data are provided free of charge by the joint Cambridge Crystallographic Data Centre and Fachinformationszentrum Karlsruhe Access Structures service.
[47] W. Li, B. Li, X. Cai, L. Gan, Z. Xu, W. Li, K. Liu, D. Chen, S. J. Su, *Angew. Chem. Int. Ed.* **2019**, *58*, 11301–11305.
[48] D. Liu, J. Y. Wei, W. W. Tian, W. Jiang, Y. M. Sun, Z. Zhao, B. Z. Tang, *Chem. Sci.* **2020**, *11*, 7194–7203, https://doi.org/10.1039/D0SC02194F.
[49] N. Peethani, N. Y. Kwon, C. W. Koh, S. H. Park, J. M. Ha, M. J. Cho, H. Y. Woo, S. Park, D. H. Choi, *Adv. Opt. Mater.* **2024**, *12*, 2301217, https://doi.org/10.1002/adom.202301217.
[50] L. Xu, H. Liu, X. Peng, P. Shen, B. Z. Tang, Z. Zhao, *Angew. Chem. Int. Ed.* **2023**, *62*, e202300492.
[51] Z. Zhong, X. Zhu, X. Wang, Y. Zheng, S. Geng, Z. Zhou, X. J. Feng, Z. Zhao, H. Lu, *Adv. Funct. Mater.* **2022**, *32*, 2112969, https://doi.org/10.1002/adfm.202112969.
[52] Y. Li, M. Zhou, Y. Niu, Q. Guo, A. Xia, *J. Chem. Phys.* **2015**, *143*, 034309, https://doi.org/10.1063/1.4926998.
[53] T. Villnow, G. Ryseck, V. Rai-Constapel, C. M. Marian, P. Gilch, *J. Phys. Chem. A* **2014**, *118*, 11696–11707, https://doi.org/10.1021/jp5099393.
[54] M. S. Lin, S. J. Yang, H. W. Chang, Y. H. Huang, Y. T. Tsai, Wu, S.-H. C., E. Mondal, K. T. Wong, *J. Mater. Chem.* **2012**, *22*, 16114, https://doi.org/10.1039/c2jm32717a.
[55] J. Han, P. Duan, X. Li, M. Liu, *J. Am. Chem. Soc.* **2017**, *139*, 9783–9786, https://doi.org/10.1021/jacs.7b04611.

Manuscript received: November 04, 2025
Revised manuscript received: December 10, 2025
Manuscript accepted: December 10, 2025
Version of record online: December 18, 2025